UC Santa Cruz
UC Santa Cruz Previously Published Works

Title
Epitaxial strain and the magnetic properties of canted antiferromagnetic perovskite NaNiF3 thin films

Permalink

Journal
APL Materials, 8(1)

ISSN
2166-532X

Authors
Morley, Sophie A
Marquez, Humberto
Lederman, David

Publication Date
2020

DOI
10.1063/1.5126601

Peer reviewed

Epitaxial strain and the magnetic properties of canted antiferromagnetic perovskite NaNiF$_3$ thin films

Sophie A. Morley,[1] Humberto Marquez,[1] and David Lederman[1]

University of California Santa Cruz, Physics Department, 1156 High Street, Santa Cruz, CA 95064,
USA

The perovskite crystal structure is known to exhibit a multitude of interesting physical phenomena owing to the intricate coupling of the electronic and magnetic properties to the structure. Fluoro-perovskites offer an alternative chemistry to the much more widely studied oxide materials which may prove advantageous for applications. It is demonstrated here for the first time that the antiferromagnetic perovskite fluoride, NaNiF$_3$, can be synthesized in thin film form. The films were grown via molecular beam epitaxy on SrTiO$_3$ (100) substrates to produce high quality epitaxial films in the thickness range of 5 – 50 nm. The *Pnma* structure of the films was confirmed by x-ray diffraction. There was a decrease in the out-of-plane lattice spacing from the bulk value corresponding to a maximum strain of 1.7 % in the thinnest film. Canted antiferromagnetism was measured in all films using magnetometry and a negative change in the antiferromagnetic ordering temperature of ΔT_N = - 9.1 $\pm$ 0.7 K was observed with increasing strain.

I. INTRODUCTION

Perovskite materials host a huge variety of interesting properties ranging from high temperature superconductivity[1], ferroelectricity[2], piezoelectricity[3] to both ferro- and antiferromagnetic order as well as metal-to-insulator transitions[4]. The flexibility of the bond angles within the perovskite crystal leads to an intimate connection between its exact structure and its electronic and magnetic properties. In turn, this results in the potential for high tunability of physical properties within composition ranges, heterostructures or via externally applied stimuli (such as electric field or strain), providing an exciting playground for fundamental science as well as diverse functionality.

There have been extensive studies on the oxide perovskites over the years but the fluoro-perovskites have received little attention, in comparison. Recently, fluoro-perovskites have been suggested as potential electrode materials in Li/Na-ion rechargeable batteries, demonstrating more robust chemistry and performance than their oxide counterparts.[5,6] Hollow microspheres of NaNiF$_3$ (NNF), the material of the current study, were shown to have outstanding electrode material properties.[7] Fluoroperovskites have also been proposed as an alternative candidate in the search for multiferroicity i.e. the simultaneous existence of long-range magnetic order and ferroelectricity.[8] Strained NaMnF$_3$ in particular was postulated to be magnetoelectric, where the magnetism and ferroelectricity are coupled and can be controlled by either an applied electric or magnetic field.[9–12] Much like the oxide compounds, it is desirable to create thin film samples to integrate into devices. It is important therefore to understand whether the fluoro-perovskites retain their physical properties in thin film form.

NaNiF$_3$ (NNF) shares the same crystal structure as NaMnF$_3$ but is not predicted to be ferroelectric according to theoretical calculations.[9] In bulk form, NNF was found to be a G-type antiferromagnet using neutron diffraction[13] with a weak ferromagnetic component along the *b* direction due to anti-symmetric exchange or the Dzyaloshinskii-Moriya interaction (DMI).[14,15] Coincidentally, DMI was first proposed in
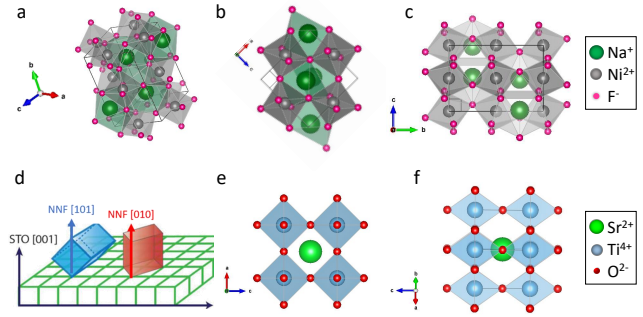

FIG. 1. (a) Schematic of the crystal structure of NaNiF$_3$ produced from VESTA software.[20] Na$^+$, Ni^{2+} and F$^-$ ions are dark green, gray and pink spheres, respectively, viewed along the (b) *b* axis and (c) *a* axis, showing the NiF$_6$ octahedra tilts and Na displacements. The unit cell is outlined in black. (d) Schematic of possible growth directions on cubic SrTiO$_3$ (STO) substrate (reproduced from ref.[11]). (e) The ideal perovskite structure of the STO, viewed along one of the cubic axes and (f) the untilted TiO$_6$ octahedra, Sr^{2+}, Ti^{4+} and O^{2-} ions are light green, blue and red spheres, respectively.

the canted antiferromagnetic fluoride, NiF$_2$[16] and not the commonly considered non-centro symmetric crystals such as the B20 compounds of MnSi[17] and FeGe[18] which are currently popular material hosts for magnetic spin textures known as skyrmions; possible future technologically viable data storage bits.[19] DMI is also present in centrosymmetric crystals when the ionic environment inversion symmetry is broken, such as is the case for the magnetic fluorides NiF$_2$ and NaNiF$_3$.

In bulk form, NNF has a distorted perovskite crystal structure with an orthorhombic *Pnma* space group symmetry. The bulk values of the lattice constants are reported as a = 5.361 Å, b = 7.688 Å and c = 5.524 Å.[21] The crystal structure can be seen in Fig. 1a-c. The distortion from an ideal perovskite structure, such as that of SrTiO$_3$ (STO), shown in Fig. 1e and f, comes from a shift of the Na atoms in the $a-b$ plane (Fig. 1b) and a tilting of the NiF$_6$ octahedra (Fig. 1c). The tilt angle has been measured in the bulk material as 11° using x-
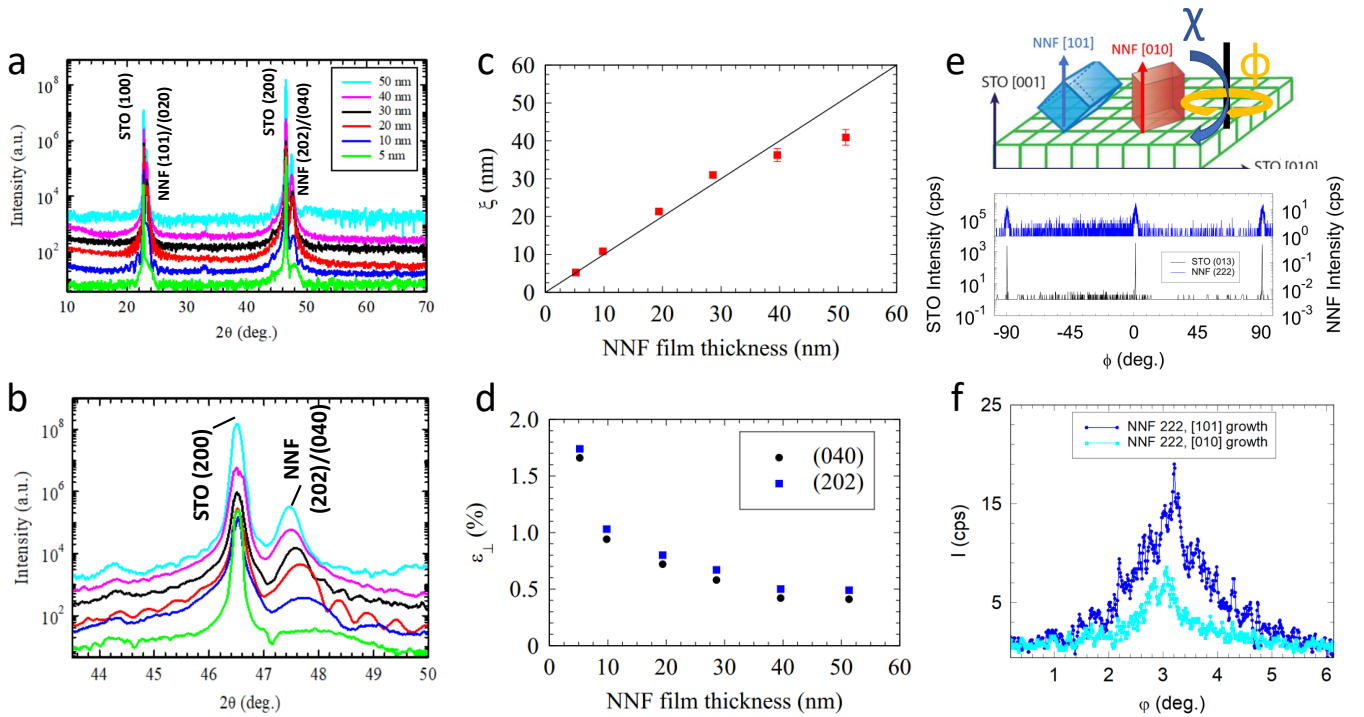
FIG. 2. (a) Full XRD patterns of NaNiF$_3$ films grown via MBE for different film thicknesses (smoothed). (b) XRD of the STO (200) and NNF (202)/(040) peaks, showing the shift in peak position as a function of thickness. (c) Plot of out-of-plane (OOP) crystallite coherence length, ξ, versus film thickness as extracted from the Scherrer fits of the XRD film peaks. Black line indicates the linear relationship for a fully coherent film. (d) The misfit strain, ε_{hkl}, as a function of film thickness, calculated for both the (040) and (202).(e) Schematic of the χ and ϕ axes used to determine the growth direction and an extended ϕ scan for the STO (013), plotted in black, and NNF (222), plotted in blue. (f) ϕ scans for the NNF (222) planes when χ was set to values corresponding to the [101] and [010] oriented growth.

ray diffraction measurements, and although this value is quite large, the distortion of the octahedra was found to be relatively small with the Ni-F-Ni bond angles within the octahedra remaining close to orthogonal.[22]

II. MATERIALS AND METHODS

A. Thin film growth

The NNF thin films were grown on pre-polished single crystal (001) STO substrates ($a = 3.905$ Å) by molecular beam epitaxy (MBE) in the thickness range 5 – 50 nm. A standard procedure to obtain an atomically flat and TiO$_2$-terminated substrate surface was used which consisted of two thermal annealing steps and a deionized water treatment.[23] The substrates were heated to 250 °C and annealed for one hour to remove surface contaminants before growing at the same temperature. The correct stoichiometry was achieved by co-depositing NaF and NiF$_2$ using effusion cells in an ultra-high vacuum chamber with base pressure $p = 3 \times 10^{-9}$ Torr and typical growth rates of 0.009 nm/s.

B. Structural and magnetic characterization

Structural characterization was carried out via X-ray diffraction (XRD) using a Rigaku Smartlab 3 kW sealed tube x-ray source with a Ge(220) crystal monochromator optimized for Cu K$_\alpha$ radiation ($\lambda = 0.15406$ nm). We also carried out in-situ analysis of the substrate and film surfaces using reflection high energy electron diffraction (RHEED) STAIB RH 15 system with an operating voltage of 15 keV corresponding to ≈ 0.01 nm de Broglie wavelength and a current of 1.5 A. In addition, we carried out ex-situ analysis of the thickness and surface roughness using X-ray reflectivity (XRR) and the surface morphology was studied by atomic force microscopy (AFM) on an Asylum Cypher S using tapping mode in air or a controlled N$_2$ atmosphere. Elemental analysis was carried out using a LEO VP1400 scanning electron microscope (SEM) with an Oxford x-ray spectrometer for electron dispersive x-ray spectroscopy (EDS). Measurements were taken with a beam energy of 25 keV and the spectra were averaged over five scans.

Magnetization measurements were performed using a Magnetic Properties Measurement System (MPMS) based on a superconducting quantum interference device (SQUID) sensor from Quantum Design.
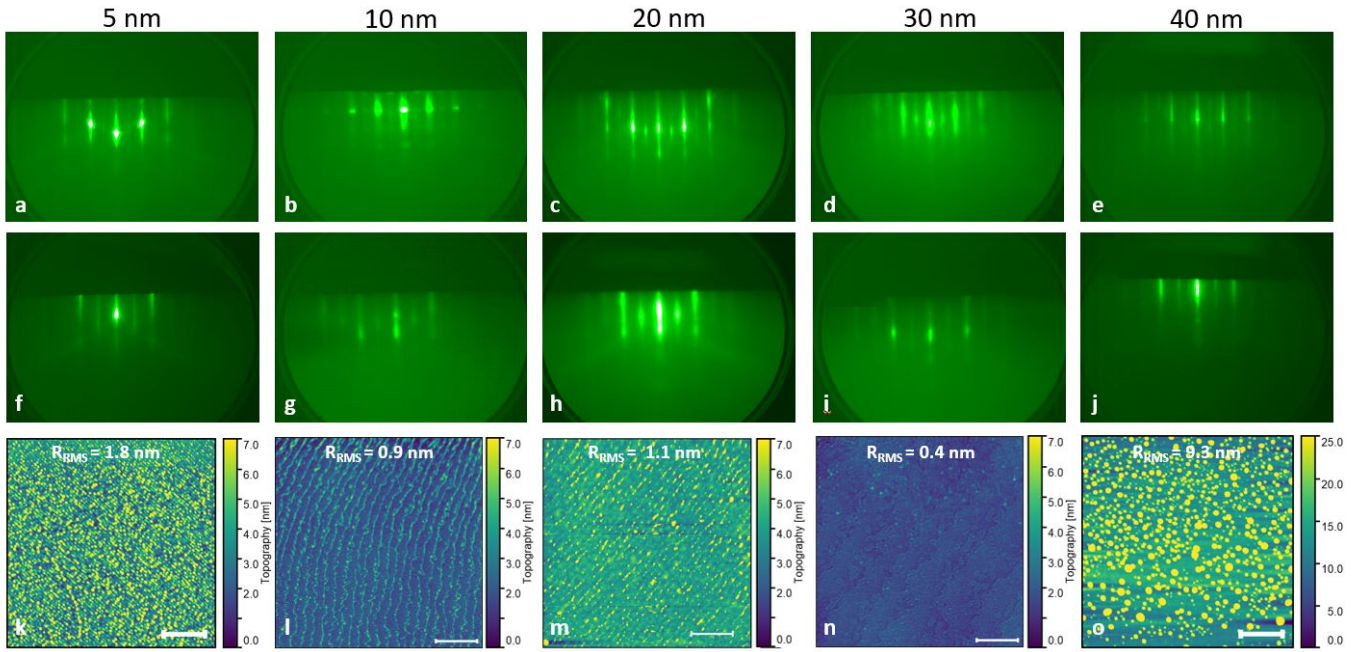
FIG. 3. RHEED images of 5, 10, 20, 30 and 40 nm with the incoming beam in the direction parallel to STO 100 (a-e) and 110 (f-j), respectively. A $10 \times 10 \ \mu m^2$ AFM topographic image for the corresponding films with increasing thickness (k-o) where all of the height color bars represent a 7 nm range, except for the 40 nm film where the range is 25 nm. Root mean square roughness (R_{RMS}) is labelled for each image. All scale bars for the AFM images are 2 μm.

III. RESULTS AND DISCUSSION

A. Structural properties

The out-of-plane XRD is shown in Fig. 2a and confirms all the films are single phase and have the expected *Pnma* structure. Only peaks related to the NNF and STO substrate were observed as labelled in the figure. An enlarged plot in Fig. 2b shows the clear shift to the right with decreasing thickness of the NNF (202)/(040) peak. In the pseudo-cubic (pc) unit cell of NNF, the corresponding lattice parameters are $a_{pc} = c_{pc} = a_0^2 + c_0^2/2 = 3.849$ Å and $b_{pc} = b_0/2 = 3.844$ Å. When grown on STO it would have a lattice mismatch strain of $\approx 1.44\%$ if the growth is oriented along the [010] orientation, with the long b axis out of the plane and the ac plane at 45 ° to the cubic STO (Fig. 1d, red unit cell). By comparison, the strain for [101]-oriented growth, with the long b-axis in the plane (Fig. 1d, blue unit cell), is also tensile but slightly increased, $\approx 1.56\%$. These two most favorable growth orientations are indistinguishable in the out-of-plane XRD, a fact encountered when growing NaMnF$_3$ on STO previously.[11] We used $\chi - \Phi$ measurements to determine the dominant growth direction. A schematic illustrating both axes with respect to the sample plane is shown in Fig. 2e along with the extended phi range showing the STO (013) and NNF (222) diffraction peaks observed every 90 °, showing that the sample is twinned in the plane. Plotted in Fig. 2f is the NNF (222) peak intensity in a Φ scan with $\chi = 63.42°$ assuming the [010] growth direction and $\chi = 26.66°$, assuming the [101] growth direction. We determined the predominant growth direction to be [101] with

orthogonal twinning in-plane and a much smaller contribution from [010] domains (between 0-20% for all samples).

The peak positions were fitted to a gaussian line shape to extract the exact 2θ position in order to calculate the out-of-plane crystallite coherence, ξ_{OOP} using the Scherrer equation:

$$\xi_{OOP} = \frac{\kappa \lambda_{Cu_{K-\alpha}}}{FWHM \cos(\theta)}, \tag{1}$$

where κ is the shape factor taken to be 0.9[24], λ is the wavelength of the x-rays ($\lambda_{Cu_{K-\alpha}} = 0.15406$ nm), FWHM is the full width half maximum of the fitted 2θ peak and θ is half of the fitted center of the peak. The thickness dependent coherence is plotted in Fig. 2c and shows that all films grown are coherent throughout their entire thickness up to 30 nm where it then starts to decrease. All thicknesses were measured directly by fitting the XRR data and the fully coherent linear relation has been plotted as a black line in the figure.

To characterize the strain in the films, the fitted 2θ positions were converted to their corresponding out-of-plane d_{hkl} spacing, assuming both growth directions, and subsequently compared to that of bulk NNF[25] to calculate the out-of-plane strain, $\varepsilon_\perp$:

$$\varepsilon_\perp = \frac{d_{hkl} - d_{hkl}^{bulk}}{d_{hkl}^{bulk}}, \tag{2}$$

where d_{hkl} is the measured interplanar spacing and d_{hkl}^{bulk} is the bulk value calculated using lattice constants from the literature.[21] We calculated this strain to be tensile (positive) and to decrease as the thickness of the film increases, by 1.2%

over the thickness range measured, as shown in Fig. 2d. The strain values saturated for the thickest films, 40 and 50 nm. Additional characterization of the in-plane crystallographic order was done via rocking curves shown in Supplementary S1.

B. Surface roughness

In-situ RHEED analysis revealed a high level of in-plane order at the surface as shown by the diffraction patterns in Fig. 3a-j. The sharp rods indicate high in-plane crystal order and also that the surfaces of the films were smooth. The topography of each film was also measured ex-situ using AFM, shown in Fig. 3k-o. The underlying terraces from the STO are visible in all samples indicating the growth was extremely smooth. Spots on the surface were confirmed using scanning electron microscopy-electron dispersive x-ray spectroscopy (SEM-EDS) as excess NaF, although this did not seem to affect the structural or magnetic properties of the underlying material. X-ray reflectivity (XRR) was used as an additional method to determine the sample roughness (ex-situ) which is shown in Fig. 4a where the data points were fitted using the GenX software.[26] All samples show Kiessig oscillations that extend to high angle and the fitted roughnesses were between 0.27 and 0.56 nm. These values have been plotted with the root mean square roughness extracted from the AFM data (Fig. 3k-o) and are shown in Fig. 4b. The roughness parameters, as determined by the two methods, are in good agreement for the 10, 20 and 30 nm films but the value from XRR is consistently lower than that of the AFM. The 10, 20 30 nm film are fairly free of defects, as seen in Fig. 3 (l) - (n), meaning the defects present are most likely only weakly interacting with the x-rays. The discrepancy arises as XRR is more sensitive to the roughness within the terraces, which have an approximate step size equal to the STO lattice constant of 0.39 nm, as this is where the material is deposited. The AFM is also sensitive to the roughness between the terraces which can be much larger than along the terraces as is shown and discussed in more detail in Supplementary S2.

C. Magnetic properties

The magnetisation was measured via zero-field-cooled and field-cooled (ZFC-FC) measurements as shown for the 20 nm film in Fig. 5a. The sample was first cooled in zero field ($H = 0$ Oe) to $T = 5$ K, after which a measurement field of $H = 1$ kOe was applied and the magnetic moment was measured while warming up to 300 K (ZFC portion of the curve). The measurement was than continued whilst cooling back down to 5 K to obtain the field-cooled portion of the curve. Subsequently, the field was set to zero and the magnetic moment was measured whilst warming back to room temperature, resulting in the thermo-remanent magnetization (TRM) plotted in Fig. 5b. The sharp increase in the susceptibility in the the ZFC data at T_N, shown more clearly in the inset of Fig. 5a, is a signature of canted antiferromagnetism
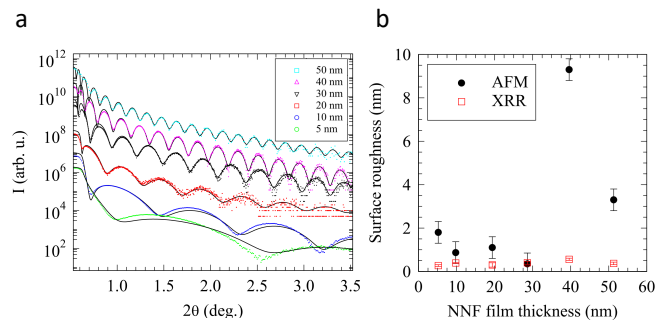

FIG. 4. (a) X-ray reflectivity (XRR) for the different thickness films showing Kiessig oscillations, the plots have been offset in intensity for clarity. The fits to the data are the solid black curves. (b) A comparison of the measured surface roughness as a function of film thickness, using XRR and atomic force microscopy (AFM).

(*i.e.* weak ferromagnetism).[15] Similar behavior has also been observed in $NaMnF_3$ thin films.[11] The weak ferromagnetic moment is due to the canting of the Ni spins away from the antiferromagnetic axis (Fig. 5c and d) and is shown as an increase in the magnetic signal as the temperature is reduced in the FC magnetisation and TRM measurement. The magnetic structure only allows canting along the b axis and is such that the canted moment for the [101]-growth direction would have a net magnetisation in-plane whereas for the [010]-growth direction it would be out-of-plane, as illustrated in Fig. 5c and d. The TRM measurements for different in-plane angles and the out-of-plane orientation of the field are shown in Fig. 5b. The data show a larger TRM moment in-plane which is in agreement with the predominant growth orientation being [101] found from XRD. We see no discernible difference between the magnetisation for the 0, 45 and 90 ° in-plane orientations (Fig. 5b) which supports the in-plane x-ray ϕ scans and the orthogonal twinning of the [101]-oriented crystal. In the magnetic measurement the ratio of the in-plane to out-of-plane magnetization is ≈ 28.5 % (assuming equal proportion of twinned domains in the plane), which is slightly higher than the ratio of (010)/(101) domains found in the in-plane XRD measurements which was 20%. This difference could be due to a small angular misalignment in the SQUID giving an in-plane component during the out-of-plane measurement.

The spontaneous magnetic moment of the NNF corresponds to a tiny fraction of the Ni^{2+} ion moment (assuming $2.0\mu_B$ per Ni) and was found to be 0.07 ± 0.02 μ_B/f.u. (using the average $M_{TRM}(T = 5$ K) value for all films except 5 nm). We also assumed that as the thin film sample is twinned in-plane we only measure half of the true bulk value in one crystalline in-plane direction. This corresponds to an upper limit of 3.5 ± 0.7% Ni^{2+} ion moment. This is in good agreement with the 3% value found in the bulk.[21] The small contribution from the (010) domains should act to reduce the measured value. It is worth noting here that if the mechanism for the canting is antisymmetric exchange, then it has been proposed that the canting angle has no temperature dependence, whereas the single ion anisotropy model does predict a tem-

perature dependence.[13]

All samples showed a qualitatively similar behaviour except the 5 nm film as shown in Fig. 6a. The thinnest film had a large ferromagnetic signal which was present up to the highest temperature measured. There was a ≈ 0.5 emu/cc = 0.01 μ_B/f.u. change in the ZFC-FC magnetisation at T = 146.4 K which we attribute to NNF. The antiferromagnetic Néel ordering temperature, T_N, was measured for the other samples as the point where the spontaneous canted moment disappeared in the TRM, as shown in Fig. 6b. We observe a thickness dependence, as shown in Fig. 6c, with a change of ΔT_N = -9.1 $\pm$ 0.7 K as the film thickness is reduced from 50 nm to 5 nm. There is a sharp change between 5 and 20 nm into a gradual plateau between 40 and 50 nm, as shown by the red curve in Fig. 6c which correlates with the calculated strain, plotted by the blue curve. Both show a plateau at the high end of the thickness range. Beyond 30 nm the sample is no longer fully strained and it has relaxed, also indicated by the difference between the out-of-plane structural coherence length and film thickness, shown in Fig. 2c. The ordering temperature of the films approaches the bulk value as the strain is reduced, shown in Fig. 6d.

There are two mechanisms whereby tensile strain can be accommodated in perovskite materials, both are shown in the lower part of Fig. 6e. The magnitude of the tilt can change through rigid rotations of the NiF$_6$ octahedra where the intra-octahedral Ni-F distances remain unchanged but there is a change in the inter-octahedral bond angle, shown as α in the figure.[27] Alternatively, a change of the in-plane Ni-F bond lengths can occur and the octahedra are distorted. It is also possible to have a combination of both simultaneously. It is well known from the Goodenough-Kanamori rule that the magnetic superexchange interaction is antiferromagnetic for the 180° transition metal-oxygen-transition metal bond angle.[28,29] A reduction in the bond angle has been shown to lower the Néel temperature in oxide perovskites and was attributed to the weakening of the Fe-O-Fe exchange interaction in the orthoferrites.[30] It is possible the reduction in T_N observed here is due to the strain being accomodated in a similar way. There is a octahedral rotation about an axis parallel to the substrate plane (labelled β in the figure) and a corresponding decrease in α, away from the ideal antiferromagnetic 180° Ni-F-Ni bond angle.

IV. CONCLUSION

In summary, highly ordered thin films of NaNiF$_3$ have been grown for the first time. The *Pnma* crystal structure was confirmed via XRD in the preferred [101] growth orientation. The films showed a reduction in the out-of-plane d spacing, which was sustained throughout the film in thicknesses up to 30 nm, after which the structure relaxed towards the bulk NNF as did the magnetic ordering temperature, T_N. The canted antiferromagnetic order was confirmed via magnetometry and the measured value of magnetisation was in good agreement with the bulk value. We attribute the decrease in T_N to increasing strain which can be accommodated

via octahedral rotations, reducing the bond angle between octahedra and causing a corresponding reduction of the super-exchange interaction across the Ni-F-Ni bonds. A detailed study of the strain-dependent bond angle is desirable which could be done using synchrotron XRD where there is sensitivity to the half order peaks created by the tilt pattern and changes can be quantified.[31] The presence of ferromagnetic behavior in the thinnest film warrants further investigation. Potential for magneto-electric coupling in strained fluoroperovskites is possible due to the predicted behavior of NaMnF$_3$, which may manifest in electric field dependent exchange bias phenomena[32] and the feasibility of ultrafast and low power spintronic devices based on antiferromagnetic insulators.[33]

[1] J. Bednorz and K. Muller, "Perovskite-type oxides - the new approach to high-TC superconductivity," Rev. Mod. Phys. **60**, 585–600 (1988).
[2] R. E. Cohen, "Origin of ferroelectricity in perovskite oxides," Nature **358**, 136–138 (1992).
[3] K. Uchino, "Glory of piezoelectric perovskites," Science and Technology of Advanced Materials **16**, 046001 (2015).
[4] Z. Liao, N. Gauquelin, R. J. Green, K. Müller-Caspary, I. Lobato, L. Li, S. Van Aert, J. Verbeeck, M. Huijben, M. N. Grisolia, V. Rouco, R. El Hage, J. E. Villegas, A. Mercy, M. Bibes, P. Ghosez, G. A. Sawatzky, G. Rijnders, and G. Koster, "Metal–insulator-transition engineering by modulation tilt-control in perovskite nickelates for room temperature optical switching," Proceedings of the National Academy of Sciences **115**, 9515–9520 (2018).
[5] W. Shi, R. Ding, X. Li, Q. Xu, D. Ying, Y. Huang, and E. Liu, "Bimetallic co-mn perovskite fluorides as highly-stable electrode materials for supercapacitors," Chemistry – A European Journal **23**, 15305–15311 (2017).
[6] D. Cao, C. Yin, C. Shi, Z. Fu, J. Zhang, and C. Li, "Cubic perovskite fluoride as open framework cathode for na-ion batteries," Advanced Functional Materials **27**, 1701130 (2017).
[7] N. Hussain, F. Wu, W. Younas, and L. Xu, "Hollow sphere formation by the self aggregation of perovskite fluoride nanif3 nanocrystals and the application of these spheres as an electrode in an ultrahigh performance asymmetric supercapacitor," New J. Chem. **43**, 11959–11967 (2019).
[8] J. F. Scott and R. Blinc, "Multiferroic magnetoelectric fluorides: why are there so many magnetic ferroelectrics?" Journal of Physics: Condensed Matter **23**, 113202 (2011).
[9] A. C. Garcia-Castro, N. A. Spaldin, A. H. Romero, and E. Bousquet, "Geometric ferroelectricity in fluoroperovskites," Physical Review B **89**, 104107 (2014).
[10] A. Garcia-Castro, A. Romero, and E. Bousquet, "Strain-Engineered Multiferroicity in P n m a NaMnF 3 Fluoroperovskite," Physical Review Letters **116**, 117202 (2016).
[11] A. KC, P. Borisov, V. V. Shvartsman, and D. Lederman, "Weak ferromagnetism and short range polar order in NaMnF3 thin films," Applied Physics Letters **110**, 092901 (2017).
[12] M. Yang, A. Kc, A. C. Garcia-Castro, P. Borisov, E. Bousquet, D. Lederman, A. H. Romero, and C. Cen, "Room temperature ferroelectricity in fluoroperovskite thin films," Scientific reports **7**, 7182 (2017).
[13] A. Epstein, J. Makovsky, M. Melamud, and H. Shaked, "Magnetic Structure of NaNi F 3," Physical Review **174**, 560–561 (1968).
[14] I. Dzyaloshinsky, "A thermodynamic theory of "weak" ferromagnetism of antiferromagnetics," Journal of Physics and Chemistry of Solids **4**, 241–255 (1958).
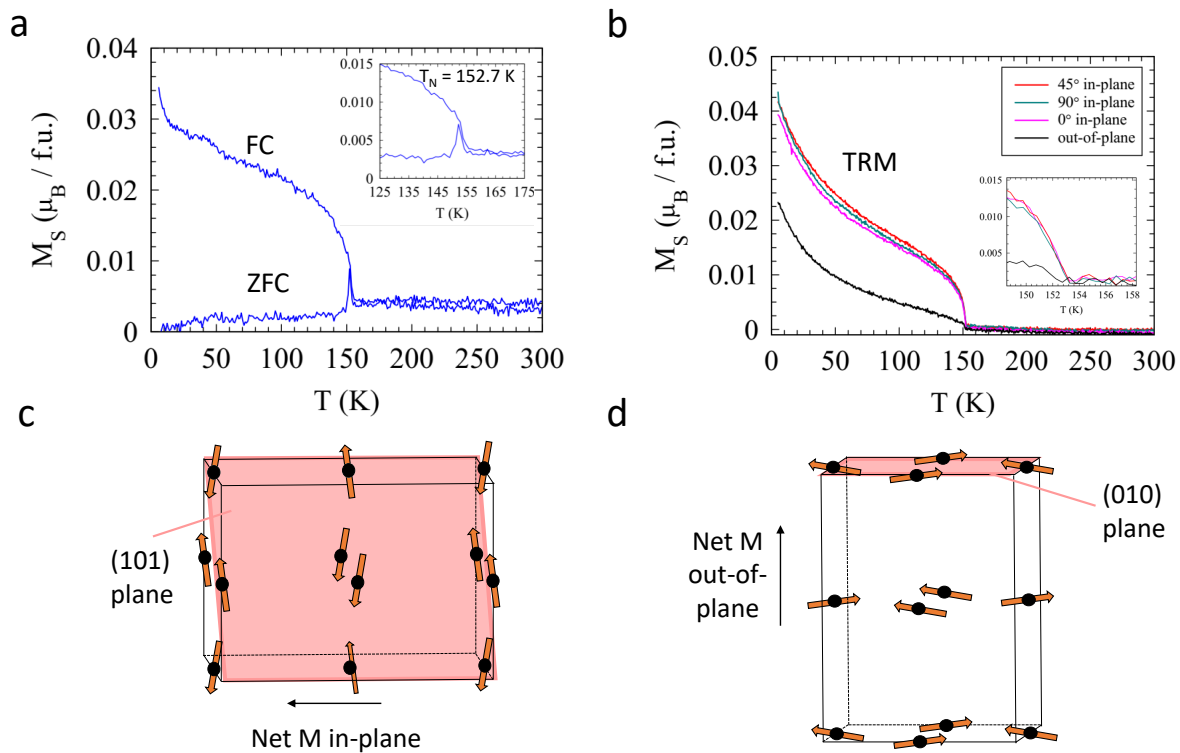
FIG. 5. (a) Zero-field-cooled (ZFC) and field-cooled (FC) magnetization as a function of temperature for the 20 nm film where the the magnetic field was applied in-plane of the film. (Inset) Enlarged area of ZFC-FC near the ordering temperature, T_N. (b) The thermal-remanent magnetization (TRM) as a function of temperature shows there is a larger magnetization for all in-plane directions and a reduced magnetization in the out-of-plane orientation. (c) Canted moments (orange arrows) of the Ni sites (black circles) would give a net moment in-plane for the [101] growth direction, (d) whereas it would have a out-of-plane moment for the [010] growth direction. The canting angle has been exaggerated for illustrative purposes.

[15] T. Moriya, "Anisotropic Superexchange Interaction and Weak Ferromagnetism," Physical Review **120**, 91–98 (1960).

[16] T. Moriya, "Theory of Magnetism of Ni F 2," Physical Review **117**, 635–647 (1960).

[17] S. Mühlbauer, B. Binz, F. Jonietz, C. Pfleiderer, A. Rosch, A. Neubauer, R. Georgii, and P. Böni, "Skyrmion Lattice in a Chiral Magnet," Science **323** (2009).

[18] X. Z. Yu, N. Kanazawa, Y. Onose, K. Kimoto, W. Z. Zhang, S. Ishiwata, Y. Matsui, and Y. Tokura, "Near room-temperature formation of a skyrmion crystal in thin-films of the helimagnet FeGe," Nature Materials **10**, 106–109 (2011).

[19] A. Fert, V. Cros, and J. Sampaio, "Skyrmions on the track," Nature Nanotechnology **8**, 152–156 (2013).

[20] K. Momma and F. Izumi, "VESTA3 for three-dimensional visualization of crystal, volumetric and morphology data," Journal of Applied Crystallography **44**, 1272–1276 (2011).

[21] S. Ogawa, "Weak Ferromagnetism of NaNiF 3," Journal of the Physical Society of Japan **15**, 2361–2361 (1960).

[22] M. Hidaka and M. Ono, "The Crystal Structure of NaNiF₃," Journal of the Physical Society of Japan **43**, 258–263 (1977).

[23] J. G. Connell, B. J. Isaac, G. B. Ekanayake, D. R. Strachan, and S. S. A. Seo, "Preparation of atomically flat SrTiO 3 surfaces using a deionized-water leaching and thermal annealing procedure," Applied Physics Letters **101**, 251607 (2012).

[24] J. I. Langford and A. J. C. Wilson, "Seherrer after Sixty Years: A Survey and Some New Results in the Determination of Crystallite Size," *J. Appl. Cryst*, **11**, 102–113 (1978).

[25] V. M. Judin and A. B. Sherman, "Magnetic Properties of NaNiF3," physica status solidi (b) **20**, 759–766 (1967).

[26] M. Björck and G. Andersson, "GenX : an extensible X-ray reflectivity refinement program utilizing differential evolution," Journal of Applied Crystallography **40**, 1174–1178 (2007).

[27] J. M. Rondinelli and N. A. Spaldin, "Structure and Properties of Functional Oxide Thin Films: Insights From Electronic-Structure Calculations," Advanced Materials **23**, 3363–3381 (2011).

[28] J. Goodenough, "Theory of the role of covalence in the perovskite-type manganites [La,M(II)]MnO3," Phys. Rev. **100**, 564–573 (1955).

[29] J. Kanamori, "Crystal distortion in magnetic compounds," Journal of Applied Physics **31**, S14–S23 (1960).

[30] I. S. Lyubutin, T. V. Dmitrieva, and A. S. Stepin, "Dependence of exchange interactions on chemical bond angle in a structural series: Cubic perovskite-rhombic orthoferrite-rhombohedral hematite," Journal of Experimental and Theoretical Physics **88**, 590–597 (1999).

[31] S. J. May, J. W. Kim, J. M. Rondinelli, E. Karapetrova, N. A. Spaldin, A. Bhattacharya, and P. J. Ryan, "Quantifying octahedral rotations in strained perovskite oxide films," Physical Review B - Condensed Matter and Materials Physics **82** (2010), 10.1103/PhysRevB.82.014110.

[32] P. Borisov, A. Hochstrat, X. Chen, W. Kleemann, and C. Binek, "Magneto-electric Switching of Exchange Bias," Physical Review Letters **94**, 117203 (2005).

[33] F. Matsukura, Y. Tokura, and H. Ohno, "Control of magnetism by electric fields," Nature Nanotechnology **10**, 209–220 (2015).
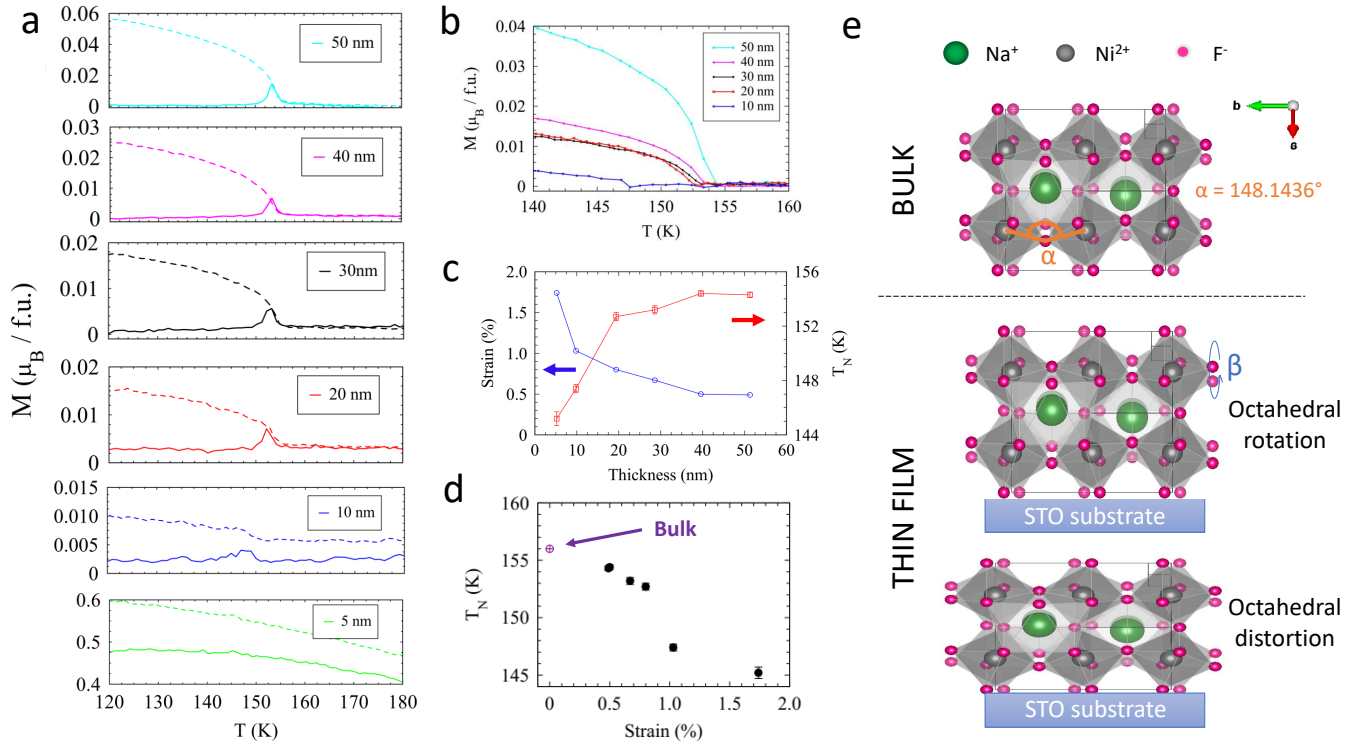
FIG. 6. Thickness dependent magnetism. (a) ZFC (solid lines) and FC (dashed lines) magnetization for each NNF thickness (b) TRM curves for each of the different thicknesses of NNF. (c) The extracted T_N and different strain values as function of film thickness. (d) The extracted T_N for different strain values, plotted along with the bulk value from the literature.[25]. (e) The NNF crystal structure for the bulk (upper) and strained thin film (lower) with the two possible ways in which the octahedra can change (rotation or distortion) to accommodate a decrease in the out of plane spacing for the [101]-oriented growth.